PHYSICAL REVIEW B **110**, 085423 (2024)

# Chiral phonon and in-plane Raman optical activity of anisotropic layered $\alpha$-MoO$_3$

Ravindra Kumar,[1,*] Prahalad Kanti Barman,[2,*] Pramoda K. Nayak,[2,3,†] and M. S. Ramachandra Rao[1,‡]

[1]*Department of Physics, Quantum Centre of Excellence for Diamond and Emergent Materials (QuCenDiEM), Nano Functional Materials Technology Centre and Materials Science Research Centre, Indian Institute of Technology Madras, Chennai 600036, India*

[2]*Department of Physics, 2D Materials Research and Innovation Group, Indian Institute of Technology Madras, Chennai 600036, India*

[3]*Centre for Nano and Material Sciences, Jain (Deemed-to-be University), Jain Global Campus,*
*Kanakapura, Bangalore 562112, Karnataka, India*

(Received 14 May 2024; revised 23 July 2024; accepted 8 August 2024; published 22 August 2024)

The interaction between electromagnetic fields and optical phonons in two-dimensional (2D) van der Waals (vdW) materials such as $\alpha$-MoO$_3$ produces a strong phonon-polariton effect within the midinfrared to terahertz frequency range. This phonon-polariton effect is highly anisotropic in nature because of the in-plane anisotropic lattice vibration of $\alpha$-MoO$_3$, which needs to be explored. In this paper, we have successfully synthesized cm-scale high-quality $\alpha$-MoO$_3$ crystals using the physical vapor deposition technique. Using helicity-resolved Raman spectroscopy, we have investigated the chiral phonon modes in $\alpha$-MoO$_3$ by varying flake thicknesses as well as a fast-hand distinction between the $A_g$ and $B_{1g}$ modes in different flake thicknesses exfoliated from the parent crystal. Our findings indicate the existence of chiral phonons in $\alpha$-MoO$_3$ and their strong dependency of chirality over the thickness of the flakes. Additionally, our analysis reveals strong in-plane anisotropy in as-grown $\alpha$-MoO$_3$, which is confirmed through angle-resolved Raman spectroscopy, and the degree of anisotropy is estimated quantitatively with respect to the thickness of the $\alpha$-MoO$_3$ flake. It is observed that the anisotropy ratio is different for different Raman modes. However, the variation of the anisotropy ratio for a particular mode is strongly dependent on the thickness of $\alpha$-MoO$_3$. Furthermore, two sets of $A_g$ modes were observed in $\alpha$-MoO$_3$ through the Raman optical activity measurements. One set of $A_g$ modes is oriented along the $a$ axis and another set along the $b$ axis. In this study of chiral phonon modes and the corresponding anisotropy along the in-plane direction, we provide valuable insights into the design of polarization-sensitive photonic devices.

DOI: 10.1103/PhysRevB.110.085423

## I. INTRODUCTION

In recent times, there has been growing interest in the investigation of the in-plane anisotropy of the two-dimensional (2D) van der Waals (vdW) materials, including black phosphorus (BP) [1], Re$X_2$ ($X$ = S, Se) [2,3], MoTe$_2$ [4], and WTe$_2$ [5], due to their low symmetry such as orthorhombic, triclinic, and monoclinic symmetries [6]. These materials exhibit exciting in-plane orientation-dependent properties which differ from the other isotropic vdW materials, and this in-plane anisotropy provides an additional parameter to control and tune their physical properties [7,8]. As a result, they have the potential for a wide range of applications, such as polarization-sensitive photodetectors [9], linearly polarized pulse generators [10], and high-gain digital inverters [11]. Although the anisotropic transition metal dichalcogenides (TMDCs) have been studied extensively, however, the nature of anisotropy in 2D transition metal oxides (TMO) has rarely been explored.

$\alpha$-MoO$_3$ belongs to the 2D TMO-based layered semiconductors with a wide band gap of ~3.0 eV and an orthorhombic structure [12]. The interaction between the electromagnetic field and the optical phonon in $\alpha$-MoO$_3$ produces phonon polaritons in the midinfrared to terahertz frequency range [13]. The phonon-polariton effect in $\alpha$-MoO$_3$ is highly anisotropic due to the anisotropic vibration of the lattice [13–15]. Therefore, it is essential to investigate the anisotropy of the lattice vibrations in $\alpha$-MoO$_3$, which can be accomplished using polarized Raman spectroscopy. In general, Raman spectroscopy is a nondestructive and fast-hand technique widely used for the characterization of vdW materials [16]. It provides information about the stacking order [17], layer thickness [18], thermal properties [19], and strength of interactions between the layers in vdW systems [20].

In comparison with unpolarized Raman spectroscopy, helicity-resolved Raman spectroscopy (HRRS) is extensively used to determine exciton/electron phonon coupling [21,22], ferromagnetism [23], quantum interference [23], and chiral phonon [24]. In HRRS, circularly polarized light is used to analyze the symmetry of the first-order Raman mode around the highest symmetric Γ point of the vdW materials [25]. Here, circularly polarized light excites the first-order Raman modes of the vdW materials, and the helicity of the scattered light from different first-order Raman modes will have the same or opposite helicity as the incident light, depending on the crystal symmetry. The helicity-selective rules of the Raman scattered light are determined by the symmetry of the crystal and the

---

[*] These authors contributed equally to this work.

[†] Contact author: pramoda.nayak@jainuniversity.ac.in

[‡] Contact author: msrrao@iitm.ac.in

lattice vibration [25]. Although HRRS can give insights of chiral phonons, it has limitations over the determination of the degree of anisotropy in low symmetric crystal structures. Angle-resolved polarized Raman spectroscopy (ARPR) is another commonly used technique to identify the Raman modes, determine the crystallographic orientation, and quantify the Raman tensor of the vdW materials [6,26].

In a recent study, Wen *et al.* [27] investigated in-plane Raman anisotropy and orientation of $\alpha$-MoO$_3$ crystals using polarized Raman spectroscopy, and a chiral phonon has been observed at the high-symmetry points of MoS$_2$, which has a hexagonal lattice [24]. However, the systematic study of chiral phonon Raman modes, as well as the in-plane Raman anisotropy with respect to the thickness of nonhexagonal lattices such as $\alpha$-MoO$_3$ flakes, is rarely explored in literature. In this paper, first, we have synthesized $\alpha$-MoO$_3$ crystals using the physical vapor deposition (PVD) technique at atmospheric pressure, followed by mechanical exfoliation of as-grown $\alpha$-MoO$_3$ crystals to get lower-thickness flakes. Thickness-dependent HRRS measurements have been carried out on the $\alpha$-MoO$_3$ flakes to know the nature of helicity Raman modes. The helicity-reversed scattering suggests the chiral nature of the phonon. Interestingly, both helicity-conserved and helicity-reversed Raman scatterings have been found in the $\alpha$-MoO$_3$ flakes, and the degree of helicity selectivity strongly depends on the thickness of the $\alpha$-MoO$_3$ flakes. The degree of helicity selectivity can also be used to distinguish the $A_g$ and $B_{1g}$ modes in $\alpha$-MoO$_3$. In addition, the thickness-dependent ARPR has been performed on the flakes to quantify the in-plane Raman modes anisotropy in $\alpha$-MoO$_3$. Our findings demonstrate another pathway to identify $A_g$ and $B_{1g}$ modes in $\alpha$-MoO$_3$ flakes and quantify the degree of anisotropy for the different Raman modes. Additionally, Raman optical activity (ROA)$_{\mathrm{C/L}}$ confirms two sets of $A_g$ modes in anisotropic $\alpha$-MoO$_3$. One set of $A_g$ modes is oriented along the *a* axis and another set along the *b* axis. However, the (ROA)$_{\mathrm{C/L}}$ measurements do not give much information for isotropic material such as MoS$_2$. By understanding the anisotropic properties of $\alpha$-MoO$_3$, one can design devices that are highly responsive to the change in polarization, making them ideal for a wide range of applications, from sensing to telecommunications.

## II. MATERIAL AND METHODS

### A. $\alpha$-MoO$_3$ growth

Here, $\alpha$-MoO$_3$ was synthesized using the PVD technique at atmospheric pressure. In a typical run, 0.1 g of MoO$_3$ (Sigma Aldrich 99.97%) precursor powder was taken in an alumina boat. This boat was kept inside an inner quartz tube, and afterward, this tube was transferred into the outer quartz tube of the tubular furnace. With the help of Ar (100 SCCM) carrier gas and a temperature of 800°C, the freestanding $\alpha$-MoO$_3$ crystals of a few centimeters were formed at the cold zone of the furnace (~30 cm away from the precursor). The schematic of the setup and optical image of $\alpha$-MoO$_3$ crystals are shown in Figs. 1(b) and 1(c). These $\alpha$-MoO$_3$ crystals were collected and reduced to lower-thickness flakes using a mechanical exfoliation technique. Thin flakes (~10–625 nm) were transferred onto a cleaned SiO$_2$ (300 nm)/Si substrate for further characterization.

### B. Characterization of $\alpha$-MoO$_3$ flakes

An optical microscope (LV10ND-Nikon) was used to identify the mechanically exfoliated $\alpha$-MoO$_3$ flakes of different thicknesses on the SiO$_2$ (300 nm)/Si substrate. X-ray diffraction (XRD) was performed by using a Rigaku smart lab x-ray diffractometer to check the crystallinity of $\alpha$-MoO$_3$ crystals. The compositional analysis was done by using energy-dispersive x-ray spectroscopy (EDS) with an FEI Inspect F field emission scanning electron microscopy (FESEM). High-resolution transmission electron microscopy (HRTEM, JEM-3010, JEOL) was used to know the in-plane lattice parameters and structure of $\alpha$-MoO$_3$. The accelerating voltage of the electron source beam was 200 kV during the measurement. Park system NX-10 atomic force microscopy (AFM) was used for measuring the $\alpha$-MoO$_3$ flake thickness with a scan rate of 0.3 Hz. The single-scan Raman spectra and mapping were performed by using a Witec alpha 300R Raman spectrometer with 532 nm laser excitation having a spot size of ~1 μm. Also, 1800 lines/mm gratings were used for all Raman measurements with a spatial resolution of ~1 cm$^{-1}$.

### C. Transmission electron microscopy sample preparation

A modified wet transfer method was used to prepare the sample for transmission electron microscopy (TEM) analysis. In general, potassium hydroxide (KOH) solution is used for the wet transfer technique, but in the case of $\alpha$-MoO$_3$, KOH reacted with the $\alpha$-MoO$_3$ flakes severely and got degraded [28]. To avoid this, we first coated a thin layer of polymethyl methacrylate (PMMA) on a cleaned SiO$_2$ (300 nm)/Si substrate and kept it dry for 24 h. Then the $\alpha$-MoO$_3$ crystal was exfoliated on PMMA-coated SiO$_2$ (300 nm)/Si substrate using scotch tape, followed by a coating of PMMA again on $\alpha$-MoO$_3$ flakes and kept 30 min for drying. The schematic is shown in Fig. S2(a) in the Supplemental Material [29] and describes the transfer process in detail. In the next step, this PMMA-coated substrate was dipped into a 2M KOH solution for 24 h, in which KOH worked as an etching agent to etch out the SiO$_2$. The floating PMMA layer containing $\alpha$-MoO$_3$ flakes was transferred into the DI water solution and kept for 24 h to clean the residual KOH. Finally, the clean $\alpha$-MoO$_3$ flakes with the PMMA layer were transferred into the TEM grid. Acetone was used to clean the PMMA from the TEM grid. The clean $\alpha$-MoO$_3$ on the Cu-mesh TEM grid was kept for 24 h for drying.

### D. HRRS and angle-resolved Raman measurements

The chiral Raman modes of $\alpha$-MoO$_3$ were measured through HRRS. For the helicity measurements of $\alpha$-MoO$_3$, the linearly polarized excitation is converted into the right-handed (RCP, $\sigma^+$) or left-handed (LCP, $\sigma^-$) circularly polarized light by placing the quarter-wave plate (with 45° or 315° angle to the principle axis) in the path of incident laser light and the sample, whereas in the detection part, the second quarter-wave plate is placed before the analyzer and the charge-coupled device (CCD) detector to select the helicity of the scattered

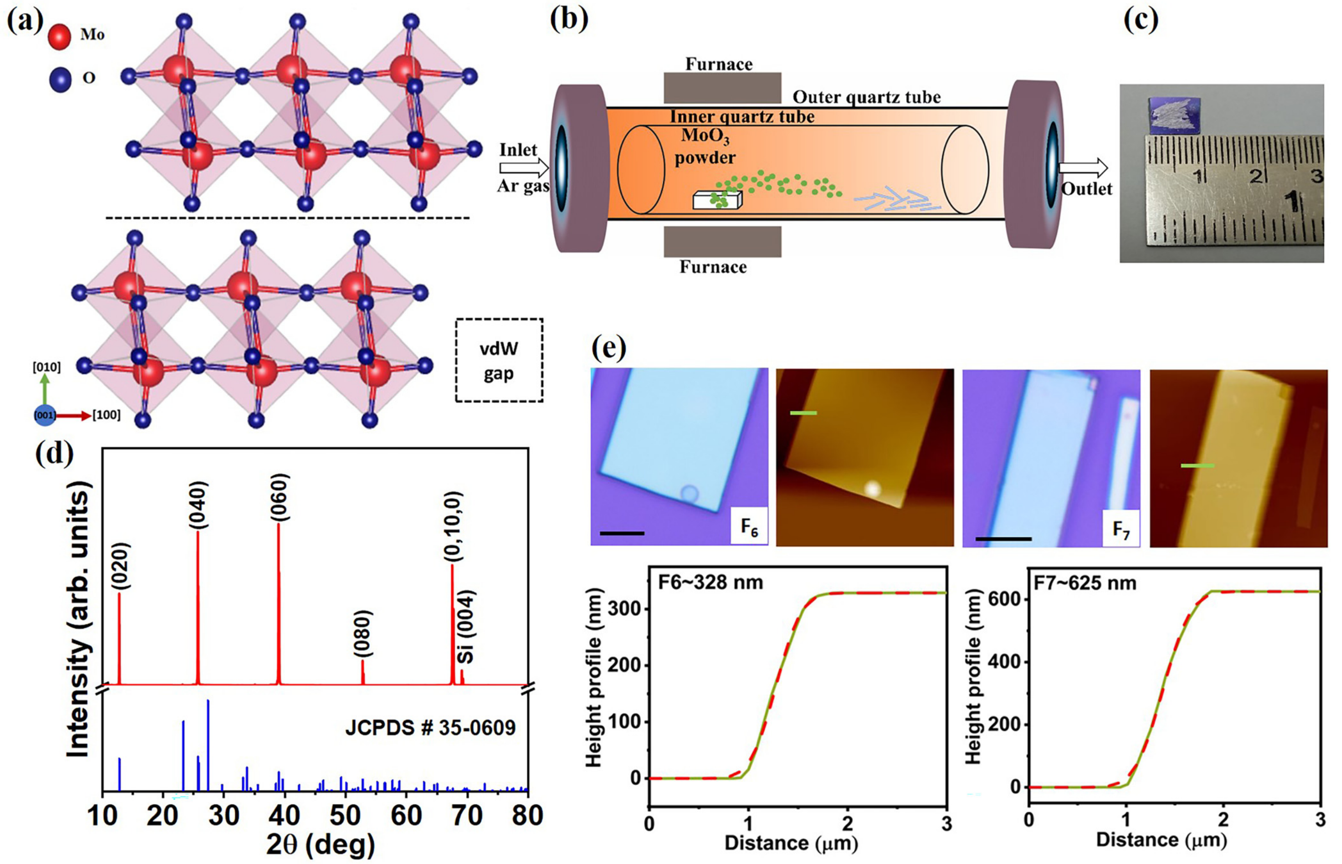

FIG. 1. (a) Crystal structure of $\alpha$-MoO$_3$ with Mo and O atoms represented as red and blue solid spheres, respectively. Mo atoms are located at the center of the octahedron of MoO$_6$. (b) Schematic showing physical vapor deposition (PVD) synthesis of $\alpha$-MoO$_3$ crystals. The light blue rectangular bar depicted in the diagram represents the resulting $\alpha$-MoO$_3$ crystals that are formed in the vicinity of the PVD chamber outlet. (c) Optical image of the as-grown cm-scale $\alpha$-MoO$_3$ crystal. (d) X-ray diffraction (XRD) pattern of the as-grown crystal along with JCPDS card No. 35-0609. (e) Optical and atomic force microscopy (AFM) images, along with the height profile of F6 and F7 flakes obtained by the mechanical exfoliation of $\alpha$-MoO$_3$ crystal. Here, the scale bar is 10 μm.

light. The schematic of the setup is shown in Fig. S6(a) in the Supplemental Material [29]. In this arrangement, the scattered RCP (LCP) light was converted to the linearly polarized component of light by the second quarter-wave plate, and these components were further selected by the analyzer and finally collected through the CCD detector. This setup allows us to measure the Raman spectra in four different configurations: $\sigma^+/\sigma^+$, $\sigma^+/\sigma^-$, $\sigma^-/\sigma^+$, and $\sigma^-/\sigma^-$. For the ARPR study, a half-wave plate was placed in the path of the incidence laser to rotate incidence laser polarization from 0° to 180°, and an analyzer (0° or 90°) was kept in the detection path for the selectively collecting the scattered light either parallel (0°) or perpendicular (90°) configuration with respect to the basal plane of $\alpha$-MoO$_3$.

## III. EXPERIMENTAL RESULTS AND DISCUSSION

$\alpha$-MoO$_3$ is a layered material with an orthorhombic crystal structure, and it belongs to the *Pbnm* space group [30]. The monolayer of $\alpha$-MoO$_3$ consists of double layers of distorted MoO$_6$ octahedra bound together via weak vdW force along the [001] axis and ionic and covalent bonds along the in-plane ([100]-[010]) atoms in $\alpha$-MoO$_3$ [31,32], as shown in Fig. 1(a). Due to weak vdW forces along the [001] axis, it can be easily peeled out layer by layer and can be down to a few layers to the monolayer limit. In this paper, we have synthesized the large area $\alpha$-MoO$_3$ crystals from the MoO$_3$ powder using the PVD method with the flow of 100 SCCM Ar gas and growth temperature of 820°C. A detailed growth process is given in the Material and Methods section. Figure 1(c) shows the centimeter-sized $\alpha$-MoO$_3$ crystal. The as-grown crystal was mechanically exfoliated to get $\alpha$-MoO$_3$ flakes of different thicknesses for further studies. The optical image as well as the height profile of the seven flakes with different thicknesses are shown in Figs. 1(e) and S1(a)–S1(e) in the Supplemental Material [29]. The thicknesses of flakes F1, F2, F3, F4, F5, F6, and F7 measured through AFM are ~10, 19, 46, 144, 172, 328, and 625 nm, respectively.

Here, we have used XRD to assess the crystallinity of as-grown $\alpha$-MoO$_3$ crystals. The XRD pattern of as-grown $\alpha$-MoO$_3$ crystal on SiO$_2$ (300 nm)/Si substrate is collected in the $2\theta$ range from 10° to 80°. The XRD peaks are located at positions ~12.7°, 25.7°, 38.9°, 52.8°, and 67.5° with the Miller indices (020), (040), (060), (080), and (0,10,0) respectively, which show good agreement with the JCPDS card data [035–0609] shown in Fig. 1(d). One can see that mostly $(0k0)$

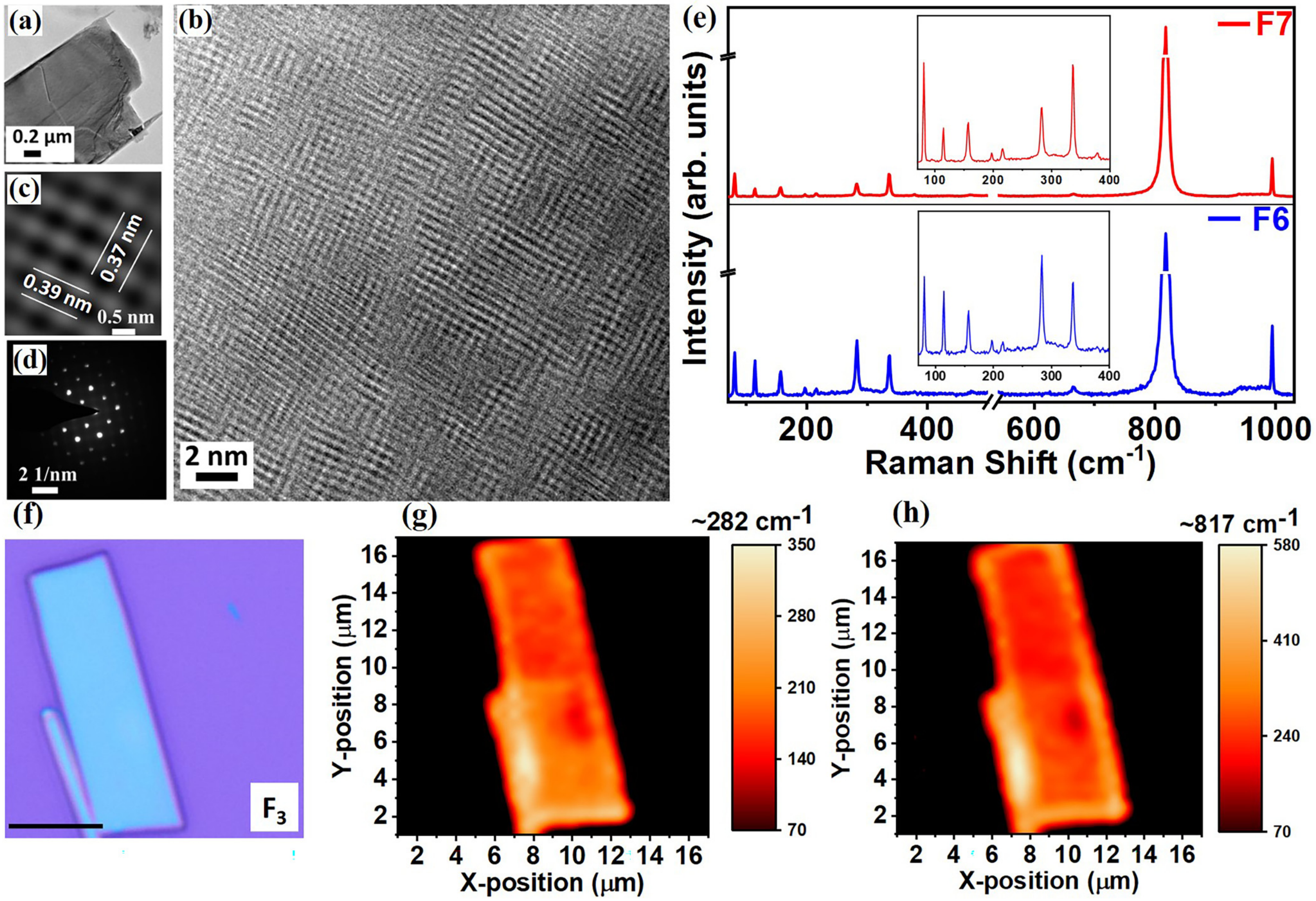

FIG. 2. (a) Low-magnified high-resolution transmission electron microscopy (HRTEM) image of the $\alpha$-MoO$_3$ flake. (b) Atomic-scale HRTEM image of the $\alpha$-MoO$_3$ flake. (c) Magnified image of the $\alpha$-MoO$_3$ flake. The parallel line corresponds to the in-plane lattice parameter of $\alpha$-MoO$_3$. (d) Selected area electron diffraction (SAED) pattern of the $\alpha$-MoO$_3$ flake. (e) Unpolarized Raman spectra of F7 and F6 flakes. The insets show the zoomed spectrum over the region of 70–400 cm$^{-1}$. (f) Optical image of the F3 flake with a scale bar of 10 µm. (g) and (h) Raman mappings correspond to 282 and 817 cm$^{-1}$ modes for the $\alpha$-MoO$_3$ flake.

peaks are present in the XRD pattern, confirming the single-crystalline nature of $\alpha$-MoO$_3$ crystals grown using the PVD technique [31].

For surface morphology and elemental composition analysis, FESEM was used with the source accelerating voltage of 30 kV. From the scanning electron microscope (SEM) image shown in Fig. S2(b) in the Supplemental Material [29], one can see that as-grown $\alpha$-MoO$_3$ crystals exhibit a layered structure with a rectangular shape. EDS measurement was carried out to know the composition analysis, as shown in Fig. S3 in the Supplemental Material [29]. The atomic percentage of Mo and O in the $\alpha$-MoO$_3$ crystal is found to be ~24 and ~76%, which confirms the stoichiometry of $\alpha$-MoO$_3$ [33].

HRTEM was performed on an $\alpha$-MoO$_3$ flake of thickness ~16 nm to know the crystal structure of $\alpha$-MoO$_3$. The low-magnified image is shown in Fig. 2(a). Figure 2(b) shows the HRTEM image of the $\alpha$-MoO$_3$ flake, and Fig. 2(c) shows the magnified image of Fig. 2(b). The in-plane lattice parameters are found to be ~0.37 and 0.39 nm, which agree well with the reported values [32]. Figure 2(d) shows the selected area electron diffraction (SAED) pattern of $\alpha$-MoO$_3$, and the rectangular pattern confirms the orthorhombic crystal structure of $\alpha$-MoO$_3$, which is consistent with previously reported patterns [32–34].

The unit cell of $\alpha$-MoO$_3$ consists of 16 atoms, and the lattice vibrations consist of 45 optical phonon branches and 3 acoustical phonon branches [27,31]. Based on the group theory, there are 24 Raman active modes in $\alpha$-MoO$_3$, i.e., $8A_g$, $4B_{1g}$, $8B_{2g}$, and $4B_{3g}$ [32]. Unpolarized Raman measurements were performed on $\alpha$-MoO$_3$ flakes with different thicknesses (F1–F7) in the range of 70–1030 cm$^{-1}$ using 532 nm laser excitation. The unpolarized Raman spectrum of flake F7 is shown in Fig. 2(e), where 11 prominent Raman modes were positioned at ~80, 113, 155, 196, 216, 282, 336, 364, 664, 817, and 993 cm$^{-1}$. It is found that some of the Raman mode intensity is compromised upon the reduction of thickness in the $\alpha$-MoO$_3$ flake due to the weak interlayer coupling of layers [30,35]. Figure 2(e) shows the Raman mode of flakes F7 and F6 with thicknesses of ~625 and 328 nm, respectively. The Raman modes of other intermediate thicknesses are shown in Fig. S4 in the Supplemental Material [29]. Detailed information about the Raman modes of $\alpha$-MoO$_3$ flakes with different flake thicknesses obtained from unpolarized Raman spectra is given in Table S1 in the Supplemental Material

[29]. In $\alpha$-MoO$_3$, the modes in the range of 1000–664 cm$^{-1}$ are attributed to the Mo-O stretching, while M=O bending modes occur in the frequency range 472–280 cm$^{-1}$, and Mo-O-Mo deformation modes occur in the range 250–80 cm$^{-1}$ [34]. The Raman modes, positioned at 113, 196, 282, and 664 cm$^{-1}$, are referred to as $B_{1g}$ modes, whereas the modes positioned at 80, 155, 216, 336, 364, 817, and 993 cm$^{-1}$ are known as $A_g$ modes [31]. Figures 2(g) and 2(h) show the Raman mapping of the two most prominent 282 and 817 cm$^{-1}$ Raman modes of flake F3 shown in Fig. 2(f). The uniformity of Raman mode intensity in mapping confirms that there is no such phase variation of the exfoliated flakes over the region of interest in this paper.

To investigate the chirality of phonon in $\alpha$-MoO$_3$, the HRRS study was carried out on different thicknesses of $\alpha$-MoO$_3$ flakes. The schematic in Fig. S6(a) in the Supplemental Material [29] shows the experimental setup for the HRRS study. In HRRS, the sample is excited with either LCP or RCP light, and scattered Raman signal, which consists of LCP and RCP components (with different percentages) of Raman modes, are detected separately. For each Raman mode, if the scattered light is copolarized with the incident light, then the chirality of the corresponding mode is conserved. On the other hand, if they are cross-polarized, then the chirality conservation is broken, which is called chirality switching. The helicity conserved scattering is referred to as ($\sigma^+/\sigma^+$ or $\sigma^-/\sigma^-$), whereas nonconserved helicity is denoted as ($\sigma^+/\sigma^-$ or $\sigma^-/\sigma^+$). In the case of TMDCs, the helicity-reversed Raman scattering at the high-symmetric point confirms the presence of chiral phonon [24,36]. The quantitative analysis of chirality has been discussed in the light of the Raman tensor in the following section.

The Raman tensor of different Raman modes in $\alpha$-MoO$_3$ can be written as [30,31]

$$R(A_{1g}) = \begin{pmatrix} a & 0 & 0 \\ 0 & b & 0 \\ 0 & 0 & c \end{pmatrix}, \tag{1}$$

$$R(B_{1g}) = \begin{pmatrix} 0 & d & 0 \\ d & 0 & 0 \\ 0 & 0 & 0 \end{pmatrix}, \tag{2}$$

$$R(B_{2g}) = \begin{pmatrix} 0 & 0 & e \\ 0 & 0 & 0 \\ e & 0 & 0 \end{pmatrix}, \tag{3}$$

$$R(B_{3g}) = \begin{pmatrix} 0 & 0 & 0 \\ 0 & 0 & f \\ 0 & f & 0 \end{pmatrix}. \tag{4}$$

The intensity of the different Raman modes in $\alpha$-MoO$_3$ can be expressed as [37]

$$I \propto \sum_j |e_s R_j e_i|^2, \tag{5}$$

where $e_i$ is the incident light polarization unit vector, $e_s$ is the scattered light unit polarization vector, and $R_j$ is the Raman tensor of the Raman mode. For the HRRS, the incident/scattered Raman vector for the right circular light $\sigma^+ = 1/\sqrt{2}(1\ i\ 0)$ and for the left circular light $\sigma^- = 1/\sqrt{2}(1\ -i\ 0)$. By employing these vectors in Eq. (5) and the corresponding Raman tensor for different modes of $\alpha$-MoO$_3$, the selection rules of the helicity-resolved Raman for $\alpha$-MoO$_3$ (when the incidence light is perpendicular to the [100]-[010] plane of the $\alpha$-MoO$_3$ flake) are

$$I(A_g)_{\text{co}} \propto \frac{|a+b|^2}{4}, \tag{6}$$

$$I(B_{1g})_{\text{co}} = 0, \tag{7}$$

$$I(B_{2g})_{\text{co}} = I(B_{3g})_{\text{co}} = 0, \tag{8}$$

$$I(A_g)_{\text{cross}} \propto \frac{|a-b|^2}{4}, \tag{9}$$

$$I(B_{1g})_{\text{cross}} \propto |d|^2, \tag{10}$$

$$I(B_{2g})_{\text{cross}} = I(B_{3g})_{\text{cross}} = 0. \tag{11}$$

Based on the selection rule, only $A_g$ and $B_{1g}$ modes should be observed in the helicity-resolved measurement, whereas $B_{2g}$ and $B_{3g}$ modes will be forbidden in this configuration; see Note S1 in the Supplemental Material [29]. Figures 3(a) and S5(a)–S5(f) in the Supplemental Material [29] show the HRRS in $\sigma^+/\sigma^+$ and $\sigma^+/\sigma^-$ configuration along with the difference in intensity between copolarization and cross-polarization configurations for the $\alpha$-MoO$_3$ flakes. It is observed that the Raman modes positioned at ∼155, 216, 336, 364, 817, and 993 cm$^{-1}$ have maximum intensity in the copolarization configuration, i.e., these modes preserve the helicity, which is incident on it. In other words, these modes are helicity-conserved Raman modes. On the other hand, Raman modes positioned at ∼113, 196, 282, and 664 cm$^{-1}$ have a maximum intensity in the cross-polarization configuration, i.e., for these modes, helicity is reversed. Also, from the figures, Raman modes corresponding to the helicity conserved in a copolarization configuration are $A_g$ modes, and the Raman modes with helicity reversed in a copolarization configuration are the $B_{1g}$ modes. These observations exactly match Eqs. (6), (9), and (10) based on the Raman tensor analysis. However, it can be noticed that, for the copolarization configuration, the intensity of the $B_{1g}$ mode should be zero, but experimentally, the $B_{1g}$ mode has a minimum with nonzero intensity in the copolarization configuration. This might be because of the nonnormal part of the laser polarization falling on the basal plane of $\alpha$-MoO$_3$ flakes, which gives rise to the nonzero intensity of these modes [38].

Additionally, from Figs. S5(e)–S5(f) in the Supplemental Material [29], for the lower-thickness flakes (F2 and F1), the Raman mode positioned at 282 cm$^{-1}$ has almost zero intensity in the copolarization configuration and the maximum intensity in cross-polarization configuration, i.e., this mode completely switches the helicity of the incident light. This is because the crystal imparts the angular momentum of the incident photon for switching the helicity of the scattered photon. Here, the helicity switching of modes points toward the chiral nature of the phonon in the $\alpha$-MoO$_3$ flakes. It is also observed that the chirality of the phonon strongly depends on the thickness of the $\alpha$-MoO$_3$ flakes. With the increase in thickness, the intensity of $B_{1g}$ modes becomes nonzero in the copolarization configuration, which can be seen in Figs. 3(a) and S5(a)–S5(d) in the Supplemental Material [29]. This thickness dependency on the chirality of the phonon suggests that the interlayer

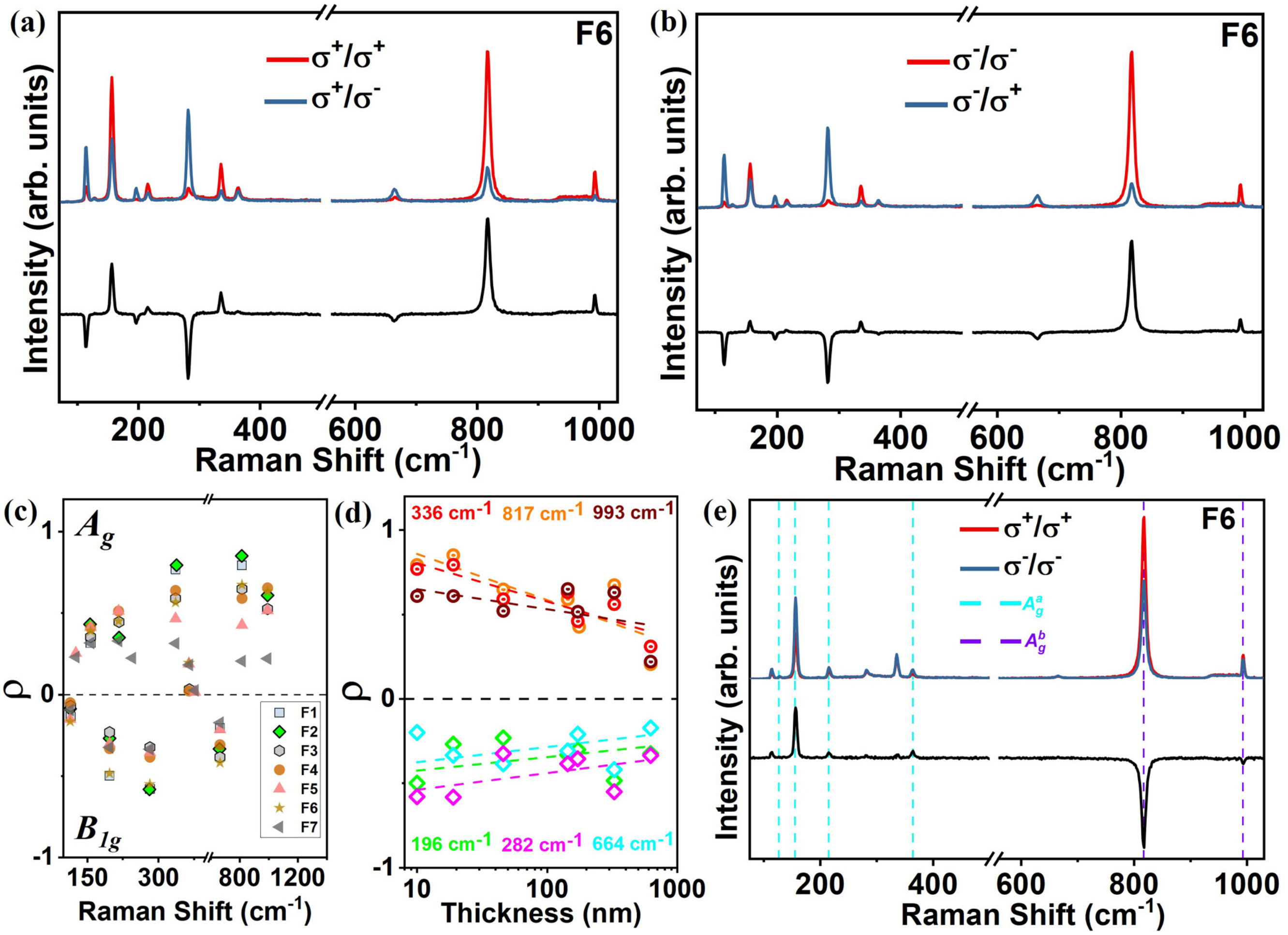

FIG. 3. (a) and (b) Helicity-resolved Raman spectra (HRRS) and corresponding intensity difference between copolarized and cross-polarized Raman scattering of the F6 flake in the range of 100–1030 $\text{cm}^{-1}$ with 532 nm laser excitation. The $\sigma^+/\sigma^+$ ($\sigma^-/\sigma^-$) and $\sigma^+/\sigma^-$ ($\sigma^-/\sigma^+$) represent the helicity-conserved and helicity-reversed Raman scattering in the $\alpha$-$\text{MoO}_3$ flakes shown by the red and blue lines, respectively, and the black color line represents the difference in intensity. (c) Degree of chirality ($\rho$) for different thicknesses of flakes as a function of Raman shift in $\sigma^+/\sigma^+$ and $\sigma^+/\sigma^-$ configuration. The $A_g$ modes show the positive value of the degree of chirality, while the $B_{1g}$ modes show the negative value of the degree of chirality. (d) Variation of the degree of chirality for different Raman modes with respect to the thickness of the $\alpha$-$\text{MoO}_3$ flakes. (e) HRRS for the F6 flake in $\sigma^+/\sigma^+$ and $\sigma^-/\sigma^-$ configurations are represented by red and blue lines, respectively. The black line represents the Raman optical activity $(\text{ROA})_\text{C}$. The $a$- and $b$-axis-oriented $A_g$ modes are shown in cyan and violet dotted lines, respectively.

interaction influences the chiral nature of the phonon in $\alpha$-$\text{MoO}_3$ [39]. Similar observations are also made in the $\sigma^-/\sigma^-$ and $\sigma^-/\sigma^+$ configurations, where we excite the sample only with LCP light and detect LCP and RCP light. This can be seen in the Figs. 3(b) and S6(b)–S6(g) in the Supplemental Material [29].

The degree of the chirality ($\rho$) of different Raman modes in $\sigma^+/\sigma^+$ and $\sigma^+/\sigma^-$ configurations for the HRRS can be expressed as [39]

$$\rho = \left(\frac{I_{\sigma^+/\sigma^+} - I_{\sigma^+/\sigma^-}}{I_{\sigma^+/\sigma^+} + I_{\sigma^+/\sigma^-}}\right), \tag{12}$$

where $I_{\sigma+/\sigma+}$ and $I_{\sigma+/\sigma^-}$ are the Raman mode intensity of copolarized and cross-polarized Raman scattering.

For all the flakes, it is found that the degree of chirality is different for different Raman modes. For all $A_g$ modes, $\rho$ has a positive value, whereas for all $B_{1g}$ modes, $\rho$ is negative in both configurations shown in Figs. 3(c) and S6(h) in the Supplemental Material [29]. The different $\rho$ values are shown in Fig. 3(c). For flake F6, the Raman modes ($A_g$ modes) positioned at ~155, 216, 336, 364, 817, and 993 $\text{cm}^{-1}$ show the helicity conservation ($\rho^+$) ~ 38, 45, 56, 19, 67, and 63%, whereas the $B_{1g}$ modes positioned at ~113, 196, 282, and 664 $\text{cm}^{-1}$ show ~16, 48, 55, and 42% helicity-reversed ($\rho^-$) degree of chirality in $\sigma^+/\sigma^+$ and $\sigma^+/\sigma^-$ configurations. For flakes F1–F7, the degree of chirality is given in Tables S2 and S3 in the Supplemental Material [29] for both configurations. From Tables S2 and S3 in the Supplemental Material [29], we found that the value of the degree of chirality is almost the same in both configurations. This indicates that the degree of chirality is independent of the configuration of the circular polarized Raman measurements. To know the thickness dependency of the degree of chirality, the experiment was carried out on the different thickness flakes. The HRRS measurements of these flakes are shown in Figs. 3(a) and 3(b), S5(a)–S5(f), and S6(b)–S6(g) in the Supplemental

Material [29], and from Figs. 3(c) and S6(h) in the Supplemental Material [29], the magnitude of $\rho$ is different for different thicknesses of the flake for a particular Raman mode. For instance, the degree of chirality of $B_{1g}$ and $A_g$ Raman modes positioned at 196, 282, 336, 664, 817, and 993 cm$^{-1}$ decreases in magnitude with respect to the thickness shown in Figs. 3(d) and S6(i) in the Supplemental Material [29] for both configurations. This is due to the interlayer coupling between the $\alpha$-MoO$_3$ layers influencing the degree of chirality [39–41]. For a detailed analysis, see Note S3 in the Supplemental Material [29]. Furthermore, as per earlier reports, the axial refractive index is different for this anisotropic $\alpha$-MoO$_3$ [33], which causes unequal light coupling with the modes, which is highly directional with the crystal axis. To show that, we have compared the two circularly polarized Raman spectra in $\sigma^+/\sigma^+$ and $\sigma^-/\sigma^-$ configurations. For the isotropic materials, the Raman mode intensity will be the same for the $\sigma^+/\sigma^+$ and $\sigma^-/\sigma^-$ configurations. To show this, we have performed these measurements on MoS$_2$, which is isotropic in nature (see Fig. S7(a) in the Supplemental Material [29]). As expected for isotropic material, both configurations show similar intensity in MoS$_2$. Surprisingly, for the anisotropic materials, in this case, $\alpha$-MoO$_3$, the $A_g$ modes show different intensity behavior in these two configurations. We defined the Raman optical activity [$(\mathrm{ROA})_\mathrm{C} = I_{\sigma^-/\sigma^-} - I_{\sigma+/\sigma+}$] derived by taking the intensity difference between the Raman spectra of $\sigma^-/\sigma^-$ and $\sigma^+/\sigma^+$ configurations. In this case, for $\alpha$-MoO$_3$, we found two sets of $(\mathrm{ROA})_\mathrm{C}$ of $A_g$ modes. One set of $A_g$ modes (126, 155, 215, and 364 cm$^{-1}$) shows a positive value of $(\mathrm{ROA})_\mathrm{C}$ (see Figs. 3(f) and S8(a)–S8(f) in the Supplemental Material [29]), and interestingly, these modes are $a$-axis-oriented Raman modes. Meanwhile, another set of $A_g$ modes (817 and 993 cm$^{-1}$) shows a negative value of $(\mathrm{ROA})_\mathrm{C}$; these are assigned as $b$-axis-oriented Raman modes. This also verifies our assumption and gives us the fast-hand and one-step method to identify the axial modes in anisotropic materials as well as provides a straightforward alternate way to distinguish different types of Raman modes and the chiral nature of the phonon in the $\alpha$-MoO$_3$ system. A detailed discussion of different axis-oriented modes is provided in the next section. This measurement technique with circularly polarized light added an extra dimension to a set of anisotropic materials to explore their axial orientation of Raman modes.

The anisotropic ratio in the Raman modes for $\alpha$-MoO$_3$ is measured using ARPR. The schematic for the ARPR study is shown in Fig. S9 in the Supplemental Material [29]. For ARPR, the incident polarized vector is $e_i = (\cos\alpha\ \sin\alpha\ 0)$, where $\alpha$ is the rotation angle between the incidence laser and the $x$ axis, and the scattered polarized unit vector is $e_s = (100)$ and (0 1 0) when the analyzer is parallel and perpendicular to the basal plane of $\alpha$-MoO$_3$, respectively. By using Eq. (5) with the appropriate Raman tensor, the intensity of the Raman modes in parallel and perpendicular configurations can be expressed as

$$I^{\parallel}(A_g) \propto (a\cos\alpha)^2, \tag{13}$$

$$I^{\parallel}(B_{1g}) \propto (d\sin\alpha)^2, \tag{14}$$

$$I^{\parallel}(B_{2g}) = I^{\parallel}(B_{3g}) = 0, \tag{15}$$

$$I^{\perp}(A_g) \propto (b\sin\alpha)^2, \tag{16}$$

$$I^{\perp}(B_{1g}) \propto (d\cos\alpha)^2, \tag{17}$$

$$I^{\perp}(B_{2g}) = I^{\perp}(B_{3g}) = 0. \tag{18}$$

The above calculation shows that only $A_g$ and $B_{1g}$ modes will have nonzero intensity; see Note S2 in the Supplemental Material [29]. The corresponding intensity variation of $A_g$ modes will provide the value of two Raman tensor elements $a$ and $b$ when the analyzer is parallel and perpendicular to the basal plane of the $\alpha$-MoO$_3$ flake, respectively. The $B_{1g}$ modes will give the value of Raman tensor element $d$, which is expected to be the same in both the parallel and perpendicular cases. Figures 4(a)–4(f) and 5(a)–5(f) show the variation of Raman mode intensity with respect to the incident laser polarization for different Raman modes of flakes F7 and F6, respectively. Both $A_g$ and $B_{1g}$ modes have different intensity variations with the incident laser polarization. The $A_{1g}$ modes have minimum intensity ~90° when the analyzer is parallel and maximum intensity when the analyzer is perpendicular. On the other hand, for the $B_{1g}$ modes, the intensity variation does not follow the same pattern as the $A_g$ mode. The intensity of the $B_{1g}$ mode is maximum/minimum ~120° when the analyzer is parallel/perpendicular. This is true for all other flakes shown in Figs. S10–S14 in the Supplemental Material [29]. The angular mismatch (~30°) between the $A_g$ max and $B_{1g}$ max clearly depicts that in-plane ([100]-[010] plane) anisotropy of $\alpha$-MoO$_3$ is highly directional and based on the axial orientation of Mo and O atoms. In contrast with isotropic materials such as MoS$_2$ and WSe$_2$, the Raman modes do not show variation in intensity with respect to the incident laser polarization [42,43]. Our intensity variation in Raman intensity with respect to the polarization angle is well fitted with Eqs. (13), (14), (16), and (17) derived from the Raman tensor analysis.

By fitting the ARPR data with Eqs. (13)–(18), it is observed that $A_g$ modes are of two kinds: case 1, where $a > b$, and case 2, where $a < b$ can be seen in Table S4 in the Supplemental Material [29]. For flakes F6 and F7, $A_g$ Raman modes positioned at ~80, 336, 817, and 993 cm$^{-1}$ have $a < b$, i.e., these Raman modes are designated as $A_g^b$ modes. The $A_g$ Raman modes positioned at ~155 and 364 cm$^{-1}$ have $a > b$, named as $A_g^a$, which are in good agreement with the previously reported studies [30,31]. It is found that the value of Raman tensor element $d$ is almost the same in both cases (when the analyzer is parallel or perpendicular) for $B_{1g}$ modes, as can be seen in Table S5 in the Supplemental Material [29]. The difference between $a$ and $b$ is due to the anisotropic atomic displacement in $\alpha$-MoO$_3$ [31]. Further, it was found that some of the Raman modes (~155 and 364 cm$^{-1}$) of flakes F6 and F5 do not follow a similar trend of intensity variation like F1, F2, F3, F4, and F7. This is due to the different relative intensity profile variation as compared with the other flakes, as shown in the inset of Fig. 2(e). Further study may need to explain such unlike behavior of those two modes. The ratio of $b/a$ is calculated to know the in-plane Raman anisotropy present in $\alpha$-MoO$_3$. It is found that the $b/a$ ratio is different for the different Raman modes and shows the periodiclike variation with respect to the thickness. The variation of the $b/a$ ratio

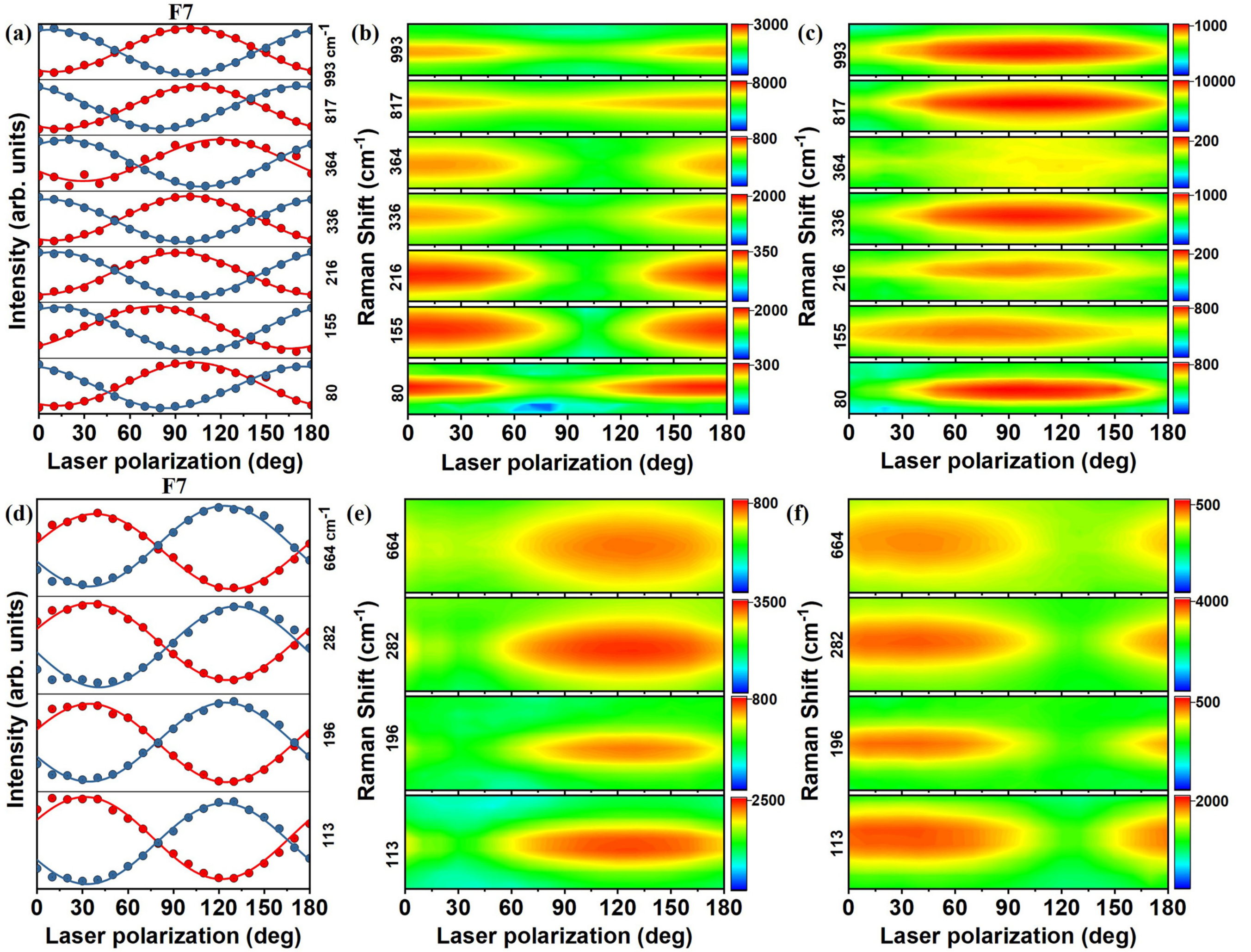

FIG. 4. (a) Intensity variation of $A_g$ Raman modes for the F7 flake as a function of incident laser polarization. (b) and (c) Color plot of $A_g$ modes when the analyzer is parallel and perpendicular to the basal plane of the $\alpha$-MoO$_3$ flake, respectively. (d) Intensity variation of $B_{1g}$ Raman modes for the F7 flake as a function of incident laser polarization. (e) and (f) Color plot of $B_{1g}$ modes when the analyzer is parallel and perpendicular to the basal plane of the $\alpha$-MoO$_3$ flake, respectively. Blue and red lines represent that the analyzer is parallel and perpendicular to the basal plane of the flake.

with respect to the thickness is shown in Fig. 6(a) for the 817 cm$^{-1}$ ($A_g^b$) and 155 cm$^{-1}$ ($A_g^a$) Raman modes. The periodiclike variation in the $b/a$ ratio of different Raman modes is because the birefringence of $\alpha$-MoO$_3$ modulates the ARPR response, which leads to the interferencelike pattern of the $b/a$ ($F_{\mathrm{en}}$) (see Note S4 in the Supplemental Material [29]) [1,44,45]. Moreover, the birefringence of $\alpha$-MoO$_3$ causes unequal light coupling with the Raman modes, which is highly directional with the crystal axis. To show that, we have again compared the two linear polarized Raman spectra in 0°/0° (excitation/detection) and 90°/90° polarization configurations. For isotropic materials such as MoS$_2$, all the intensities in 0°/0° and 90°/90° configurations will be the same, as expected [42]. We have verified this phenomenon with standard MoS$_2$ flakes, as shown in Fig. S7(b) in the Supplemental Material [29]. However, surprisingly, for the anisotropic materials, in this case, $\alpha$-MoO$_3$, the $A_g$ modes show different intensity behavior in these two configurations. We defined the Raman optical activity [$(\mathrm{ROA})_{\mathrm{L}} = I_{0^\circ/0^\circ} - I_{90^\circ/90^\circ}$] for plane-polarized light, which is derived by taking the intensity difference between the Raman spectra of 0°/0° and 90°/90° configurations. Here, one set of $A_g$ modes (126, 155, 215, and 364 cm$^{-1}$) shows a positive value of $(\mathrm{ROA})_{\mathrm{L}}$, and interestingly (see Figs. 6(b) and S15(a)–S15(f) in the Supplemental Material [29]), these modes are $a$-axis oriented. Meanwhile, another set of $A_g$ (80, 817, and 993 cm$^{-1}$) modes shows a negative value of $(\mathrm{ROA})_{\mathrm{L}}$; these modes are $b$-axis-oriented Raman modes. Here again, the in-plane direction confirmation of different modes is done in two different ways: one with Raman tensor analysis and another one through $(\mathrm{ROA})_{\mathrm{L}}$ between two sets of linearly polarized Raman spectra. In conclusion, through the $(\mathrm{ROA})_{\mathrm{C/L}}$ measurements, only two sets of Raman spectra can confirm the crystallography-axis-orientated mode rather than performing complete ARPR measurements (rotating the complete sample or laser polarization angle), which is time consuming, too. Furthermore, the ARPR data show that there is an angular mismatch between the axis-oriented modes, as can be seen in Figs. 6(c) and S16(a)–S16(f) in the Supplemental Material

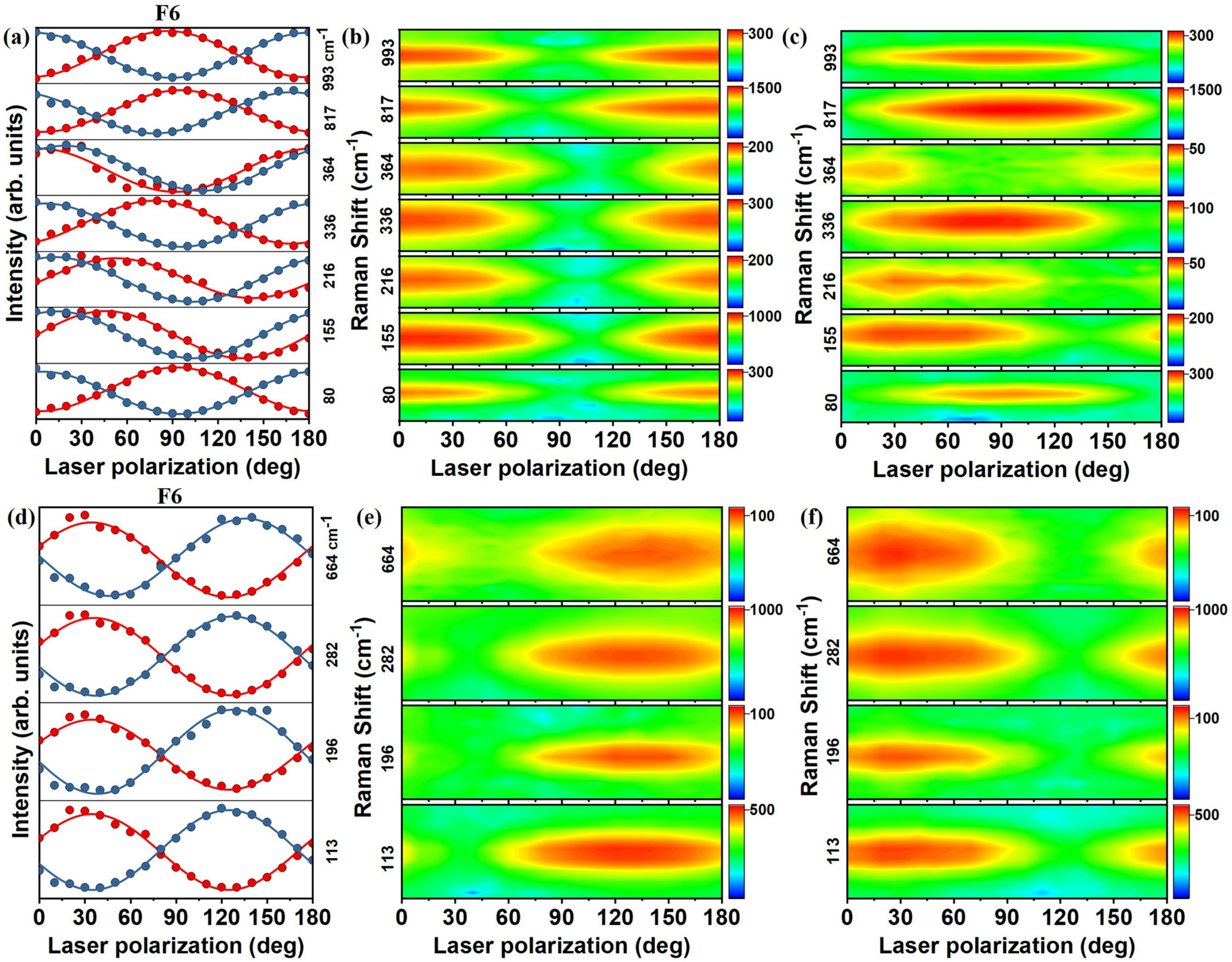

FIG. 5. (a) Intensity variation of $A_g$ Raman modes for the F6 flake as a function of incident laser polarization. (b) and (c) Color plot of $A_g$ modes when the analyzer is parallel and perpendicular to the basal plane of the $\alpha$-MoO$_3$ flake, respectively. (d) Intensity variation of $B_{1g}$ Raman modes for the F6 flake as a function of incident laser polarization. (e) and (f) Color plot of $B_{1g}$ modes when the analyzer is parallel and perpendicular to the basal plane of the $\alpha$-MoO$_3$ flake, respectively. Blue and red lines represent that the analyzer is parallel and perpendicular to the basal plane of the flake.

[29], which again concluded with the different magnitudes of the birefringence effect over the Raman modes based on crystal axis orientation in $\alpha$-MoO$_3$.

## IV. CONCLUSIONS

In summary, $\alpha$-MoO$_3$ crystals were synthesized using the PVD technique. The HRRS study was performed on the different thicknesses of the $\alpha$-MoO$_3$ flakes, which were obtained through the mechanical exfoliation of as-grown $\alpha$-MoO$_3$ crystals. It is observed that all the $A_g$ modes exhibit helicity-conserved Raman scattering, whereas $B_{1g}$ modes show helicity-reversed scattering in $\alpha$-MoO$_3$. Helicity-reversed Raman scattering indicates the presence of the chiral phonon at the high-symmetric point of the Brillouin zone. The $B_{1g}$ mode positioned at 282 cm$^{-1}$ displays the almost complete switching of the helicity of an incident photon at a lower thickness of the $\alpha$-MoO$_3$ flake, while at a higher thickness, the degree of helicity switching decreases because of the interlayer coupling effect. The ARPR study was conducted to confirm the in-plane anisotropy in the Raman modes of $\alpha$-MoO$_3$ and to distinguish between different types of Raman modes present in the material. The different values of Raman anisotropy in $A_g$ modes also classify the existence of two different kinds of Raman vibrations $A_g^a$ and $A_g^b$ based on the in-plane axial direction of the $\alpha$-MoO$_3$ crystal. Additionally, Raman optical activity (ROA)$_{\mathrm{C/L}}$ measurements provide quick information on different axis orientation Raman modes in the anisotropic $\alpha$-MoO$_3$ flakes of different thicknesses. The distinction of chiral phonon modes in $\alpha$-MoO$_3$ and its in-plane anisotropic nature can assist in the development of polarization-sensitive photonic devices and nonlinear optoelectronics.

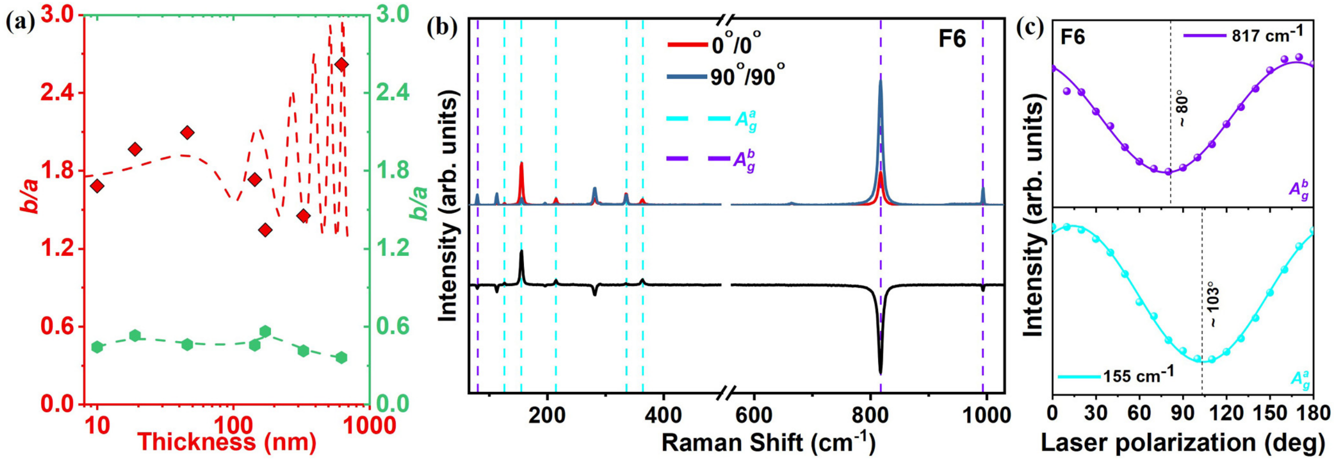

FIG. 6. (a) Variation of the Raman tensor element ratio *b*/*a* vs thickness of the $A_g$ modes (155 and 817 cm$^{-1}$) shown in green and red, respectively. The red dotted curve represents the enhancement factor ($F_{\rm en}$) profile of $\alpha$-MoO$_3$. (b) Linearly polarized Raman spectra for the F6 flake in 0°/0° and 90°/90° configurations are represented by red and blue lines, respectively. The black line represents the Raman optical activity (ROA)$_{\rm L}$. The *a*- and *b*-axis-oriented $A_g$ modes are shown in cyan and violet dotted lines, respectively. (c) Angle-resolved polarized Raman spectroscopy (ARPR) intensity variation of prominent *a*-axis-oriented (155 cm$^{-1}$) and *b*-axis-oriented (817 cm$^{-1}$) Raman mode of F6 flakes.

## ACKNOWLEDGMENTS

P.K.N. acknowledges the MHRD STARS Research Grant No. STARS/APR2019/396. P.K.N. also acknowledges the financial support from the Department of Science and Technology, Government of India (DST-GoI), with Sanction Order No. SB/S2/RJN-043/2017 under the Ramanujan Fellowship and support from the Institute of Eminence scheme at IIT-Madras, through the 2D Materials Research and Innovation Group. This paper was partially supported by DST-GoI, which led to the establishment of the Nano Functional Materials Technology Centre [No. SR/NM/NAT/02−2005 and No. DST/NM/JIIT-01/2016(C)]. M.S.R. acknowledges the support from the Institute of Eminence scheme at IIT-Madras, through the Quantum Centres of Excellence for Diamond and Emergent Materials [QuCenDiEM, IoE/CoE, Grant No. 11/9/2019-U.3(A)]. R.K. acknowledges all MSRC students and project staff for helpful discussions.

---

[1] B. Zou, Y. Wei, Y. Zhou, D. Ke, X. Zhang, M. Zhang, C. T. Yip, X. Chen, W. Li, and H. Sun, Unambiguous determination of crystal orientation in black phosphorus by angle-resolved polarized Raman spectroscopy, Nanoscale Horizons **6**, 809 (2021).

[2] D. A. Chenet, O. B. Aslan, P. Y. Huang, C. Fan, A. M. Van Der Zande, T. F. Heinz, and J. C. Hone, In-plane anisotropy in mono- and few-layer ReS$_2$ probed by Raman spectroscopy and scanning transmission electron microscopy, Nano Lett. **15**, 5667 (2015).

[3] D. Wolverson, S. Crampin, A. S. Kazemi, A. Ilie, and S. J. Bending, Raman spectra of monolayer, few-layer, and bulk ReSe$_2$: An anisotropic layered semiconductor, ACS Nano **8**, 11154 (2014).

[4] Q. Song, H. Wang, X. Pan, X. Xu, Y. Wang, Y. Li, F. Song, X. Wan, Y. Ye, and L. Dai, Anomalous in-plane anisotropic Raman response of monoclinic semimetal 1$T'$-MoTe$_2$, Sci. Rep. **7**, 17939 (2017).

[5] Q. Song, X. Pan, H. Wang, K. Zhang, Q. Tan, P. Li, Y. Wan, Y. Wang, X. Xu, M. Lin *et al.*, The in-plane anisotropy of WTe$_2$ investigated by angle-dependent and polarized Raman spectroscopy, Sci. Rep. **6**, 29254 (2016).

[6] L. Li, W. Han, L. Pi, P. Niu, J. Han, C. Wang, B. Su, H. Li, J. Xiong, Y. Bando *et al.*, Emerging in-plane anisotropic two-dimensional materials, InfoMat **1**, 54 (2019).

[7] T. Low, R. Roldán, H. Wang, F. Xia, P. Avouris, L. M. Moreno, and F. Guinea, Plasmons and screening in monolayer and multilayer black phosphorus, Phys. Rev. Lett. **113**, 106802 (2014).

[8] S. Yang, C. Hu, M. Wu, W. Shen, S. Tongay, K. Wu, B. Wei, Z. Sun, C. Jiang, L. Huang *et al.*, In-plane optical anisotropy and linear dichroism in low-symmetry layered TlSe, ACS Nano **12**, 8798 (2018).

[9] H. Yuan, X. Liu, F. Afshinmanesh, W. Li, G. Xu, J. Sun, B. Lian, A. G. Curto, G. Ye, Y. Hikita *et al.*, Polarization-sensitive broadband photodetector using a black phosphorus vertical $p-n$ junction, Nat. Nanotechnol. **10**, 707 (2015).

[10] D. Li, H. Jussila, L. Karvonen, G. Ye, H. Lipsanen, X. Chen, and Z. Sun, Polarization and thickness dependent absorption properties of black phosphorus: New saturable absorber for ultrafast pulse generation, Sci. Rep. **5**, 15899 (2015).

[11] E. Liu, Y. Fu, Y. Wang, Y. Feng, H. Liu, X. Wan, W. Zhou, B. Wang, L. Shao, C.-H. Ho *et al.*, Integrated digital inverters based on two-dimensional anisotropic ReS$_2$ field-effect transistors, Nat. Commun. **6**, 6991 (2015).

[12] S. Balendhran, S. Walia, H. Nili, J. Z. Ou, S. Zhuiykov, R. B. Kaner, S. Sriram, M. Bhaskaran, and K. Kalantar-zadeh, Two-dimensional molybdenum trioxide and dichalcogenides, Adv. Funct. Mater. **23**, 3952 (2013).

[13] G. Hu, Q. Ou, G. Si, Y. Wu, J. Wu, Z. Dai, A. Krasnok, Y. Mazor, Q. Zhang, Q. Bao *et al.*, Topological polaritons and photonic magic angles in twisted $\alpha$-MoO$_3$ bilayers, Nature (London) **582**, 209 (2020).

[14] Z. Zheng, J. Chen, Y. Wang, X. Wang, X. Chen, P. Liu, J. Xu, W. Xie, H. Chen, S. Deng *et al.*, Highly confined and tunable hyperbolic phonon polaritons in van der Waals semiconducting transition metal oxides, Adv. Mater. **30**, 1705318 (2018).

[15] Z. Zheng, N. Xu, S. L. Oscurato, M. Tamagnone, F. Sun, Y. Jiang, Y. Ke, J. Chen, W. Huang, W. L. Wilson *et al.*, A mid-infrared biaxial hyperbolic van der Waals crystal, Sci. Adv. **5**, eaav8690 (2019).

[16] R. Saito, Y. Tatsumi, S. Huang, X. Ling, and M. S. Dresselhaus, Raman spectroscopy of transition metal dichalcogenides, J. Phys.: Condens. Matter **28**, 353002 (2016).

[17] X. Luo, X. Lu, C. Cong, T. Yu, Q. Xiong, and S. Y. Quek, Stacking sequence determines Raman intensities of observed interlayer shear modes in 2D layered materials-A general bond polarizability model, Sci. Rep. **5**, 14565 (2015).

[18] Y.-S. No, H. K. Choi, J.-S. Kim, H. Kim, Y.-J. Yu, C.-G. Choi, and J. S. Choi, Layer number identification of CVD-grown multilayer graphene using Si peak analysis, Sci. Rep. **8**, 571 (2018).

[19] M. P. Singh, M. Mandal, K. Sethupathi, M. S. R. Rao, and P. K. Nayak, Study of thermometry in two-dimensional $Sb_2Te_3$ from temperature-dependent Raman spectroscopy, Nanoscale Res. Lett. **16**, 22 (2021).

[20] J.-B. Wu, M.-L. Lin, X. Cong, H.-N. Liu, and P.-H. Tan, Raman spectroscopy of graphene-based materials and its applications in related devices, Chem. Soc. Rev. **47**, 1822 (2018).

[21] Y. Zhao, S. Zhang, Y. Shi, Y. Zhang, R. Saito, J. Zhang, and L. Tong, Characterization of excitonic nature in Raman spectra using circularly polarized light, ACS Nano **14**, 10527 (2020).

[22] P. K. Barman, P. V. Sarma, M. M. Shaijumon, and R. N. Kini, Resonant-Raman study of Fröhlich exciton-phonon interaction in $WS_2$ nanostructures, Eur. Phys. J. Spec. Top. **231**, 743 (2022).

[23] B. Lyu, Y. Gao, Y. Zhang, L. Wang, X. Wu, Y. Chen, J. Zhang, G. Li, Q. Huang, N. Zhang *et al.*, Probing the ferromagnetism and spin wave gap in $VI_3$ by helicity-resolved Raman spectroscopy, Nano Lett. **20**, 6024 (2020).

[24] L. Zhang and Q. Niu, Chiral phonons at high-symmetry points in monolayer hexagonal lattices, Phys. Rev. Lett. **115**, 115502 (2015).

[25] S.-Y. Chen, C. Zheng, M. S. Fuhrer, and J. Yan, Helicity-resolved Raman scattering of $MoS_2$, $MoSe_2$, $WS_2$, and $WSe_2$ atomic layers, Nano Lett. **15**, 2526 (2015).

[26] J. Wu, N. Mao, L. Xie, H. Xu, and J. Zhang, Identifying the crystalline orientation of black phosphorus using angle-resolved polarized Raman spectroscopy, Angew. Chemie Int. Ed. **54**, 2366 (2015).

[27] M. Wen, X. Chen, Z. Zheng, S. Deng, Z. Li, W. Wang, and H. Chen, In-plane anisotropic Raman spectroscopy of van der Waals $\alpha$-$MoO_3$, J. Phys. Chem. C **125**, 765 (2020).

[28] Q. Chen, R. He, Q. Liu, Y. Wang, H. Jin, and W. Xie, Rapid preparation of large size, few-layered $MoO_3$ by anisotropic etching, Mater. Lett. **229**, 305 (2018).

[29] See Supplemental Material at http://link.aps.org/supplemental/10.1103/PhysRevB.110.085423 for OM images, AFM images, SEM image, EDS, unpolarized Raman, HRRS, ARPR, degree of chirality, and enhancement factor calculations. The Supplemental Material also contains Refs. [31,33,40,41,45].

[30] K. Kalantar-zadeh, J. Tang, M. Wang, K. L. Wang, A. Shailos, K. Galatsis, R. Kojima, V. Strong, A. Lech, W. Wlodarski *et al.*, Synthesis of nanometre-thick $MoO_3$ sheets, Nanoscale **2**, 429 (2010).

[31] Y. Gong, Y. Zhao, Z. Zhou, D. Li, H. Mao, Q. Bao, Y. Zhang, and G. P. Wang, Polarized Raman scattering of in-plane anisotropic phonon modes in $\alpha$-$MoO_3$, Adv. Opt. Mater. **10**, 2200038 (2022).

[32] B. Zheng, Z. Wang, Y. Chen, W. Zhang, and X. Li, Centimeter-sized 2D $\alpha$-$MoO_3$ single crystal: Growth, Raman anisotropy, and optoelectronic properties, 2D Mater. **5**, 45011 (2018).

[33] S. Puebla, R. D'Agosta, G. Sanchez-Santolino, R. Frisenda, C. Munuera, and A. Castellanos-Gomez, In-plane anisotropic optical and mechanical properties of two-dimensional $MoO_3$, npj 2D Mater. Appl. **5**, 37 (2021).

[34] Y. Wang, X. Guo, S. You, J. Jiang, Z. Wang, F. Ouyang, and H. Huang, Giant quartic-phonon decay in PVD-grown $\alpha$-$MoO_3$ flakes, Nano Res. **16**, 1115 (2023).

[35] A. J. Molina-Mendoza, J. L. Lado, J. O. Island, M. A. Niño, L. Aballe, M. Foerster, F. Y. Bruno, A. López-Moreno, L. Vaquero-Garzon, H. S. J. van der Zant *et al.*, Centimeter-scale synthesis of ultrathin layered $MoO_3$ by van der Waals epitaxy, Chem. Mater. **28**, 4042 (2016).

[36] E. M. Lacinska, M. Furman, J. Binder, I. Lutsyk, P. J. Kowalczyk, R. Stepniewski, and A. Wysmolek, Raman optical activity of $1T$-$TaS_2$, Nano Lett. **22**, 2835 (2022).

[37] R. Loudon, The Raman effect in crystals, Adv. Phys. **50**, 813 (2001).

[38] S. A. Ali, A. Irfan, A. Mazumder, S. Balendhran, T. Ahmed, S. Walia, and A. Ulhaq, Helicity-selective Raman scattering from in-plane anisotropic $\alpha$-$MoO_3$, Appl. Phys. Lett. **119**, 193104 (2021).

[39] C. Chen, X. Chen, B. Deng, K. Watanabe, T. Taniguchi, S. Huang, and F. Xia, Probing interlayer interaction via chiral phonons in layered honeycomb materials, Phys. Rev. B **103**, 035405 (2021).

[40] M. Koshino, Interlayer screening effect in graphene multilayers with ABA and ABC stacking, Phys. Rev. B **81**, 125304 (2010).

[41] F. Zhang, B. Sahu, H. Min, and A. H. MacDonald, Band structure of ABC-stacked graphene trilayers, Phys. Rev. B **82**, 035409 (2010).

[42] Y. Ding, W. Zheng, M. Jin, Y. Zhu, R. Zhu, Z. Lin, and F. Huang, Raman tensor of layered $MoS_2$, Opt. Lett. **45**, 1313 (2020).

[43] M. Jin, W. Zheng, Y. Ding, Y. Zhu, W. Wang, and F. Huang, Raman tensor of $WSe_2$ via angle-resolved polarized Raman spectroscopy, J. Phys. Chem. C **123**, 29337 (2019).

[44] B. Zou, X. Wang, Y. Zhou, Y. Zhou, Y. Wu, T. Xing, Y. He, J. Yang, Y. Chen, and P. Ren, Optical effect modulation in polarized Raman spectroscopy of transparent layered $\alpha$-$MoO_3$, Small **19**, 2206932 (2023).

[45] D. Yoon, H. Moon, Y.-W. Son, J. S. Choi, B. H. Park, Y. H. Cha, Y. D. Kim, and H. Cheong, Interference effect on raman spectrum of graphene on $SiO_2$/Si, Phys. Rev. B **80**, 125422 (2009).